Supplementary Material for:

Pit crater formation and caldera subsidence at Puyehue-Cordón Caulle (Chile) documented with satellite, drone, and field observations

Alonzo Olitt[α,β], Diego Lobos-Lillo[α], Matthew E. Pritchard *[α], Carolina Muñoz-Saez[α], Patrick Phelps[γ], and Philipp Ruprecht[δ]

[α] Department of Earth and Atmospheric Sciences, Cornell University, Ithaca, New York, USA.
[β] Now at: Department of Earth, Planetary, and Space Sciences, University of California, Los Angeles, Los Angeles, California, USA.
[γ] Department of Geological Sciences, California State University, Fullerton, California, USA.
[δ] Department of Geological Sciences and Engineering, University of Nevada, Reno, Nevada, USA.

This supplementary material accompanies the article:

> Olitt, A., Lobos-Lillo, D., Pritchard, M. E., Muñoz-Saez, C., Phelps, P., and Ruprecht, P. (2026) "Pit crater formation and caldera subsidence at Puyehue-Cordón Caulle (Chile) documented with satellite, drone, and field observations", *Volcanica*, *9*(2), pp. 521–537. DOI: https://doi.org/10.30909/vol/zsnc9311.

Olitt et al. (2026) should be cited if this material is used independently of the article.

S1 Geospatial Methods

S1.1 Mapping pit craters, pit crater chains, and fractures

Mapping pit craters, pit crater chains and fractures was done in `QGIS` (an open-source geographic information system software) utilizing the orthomosaic optical image and DEM obtained from the UAV. Both layers were first loaded into `QGIS`, then a new shapefile was created for each respective feature that was mapped (i.e. pit craters, pit crater chains and fractures). Polygon shapefiles were used to map pit craters and pit crater chains in order to gather morphometric measurements after mapping (e.g. diameter, depth, area, and volume), while a polyline shapefile was created to map faults and fractures. Each individual pit was mapped by adding a new polygon feature to the pit crater shapefile and assigning vertices of the polygon along the rim of the pit at increments small enough to capture the pit's essential shape. A unique numeric ID (e.g. 1, 2, 3) was assigned to each individual pit to aid identification in the analysis process. Identifying pit craters versus pseudo-pit-craters involved defining a criteria in order to be mapped. We adapted the methodology used by Kling [2020] to identify pits in Kīlauea, Hawaii and Craters of the Moon, Idaho using `ArcMap` (another GIS software). This method of pit identification seemed well suited for this study given that the data used by Kling [2020] was similarly obtained by UAV and at similar spatial resolution to the UAV data collected at PCC. Here, the criteria for classifying features as pit craters was defined as: features with easily distinguishable circular to elliptical boundaries that also exhibited some form of depression between an inverted conical or cylindrical shape when a profile tool was applied along its axis.

Mapping of pit crater chains was done similarly to pit craters. Individual pit crater chain features were drawn on top of the optical imagery by placing vertices along their boundaries at small enough increments to capture their overall shape. In most cases, vertices were placed on the edges of the semi-linear depressions formed by pit chains. However, where present, vertices were placed along the bounding faults enclosing the pit chain. In this study, pit chains were originally classified as semi-linear depressions with evidence of individual pits within the length of the depression. However, based on findings in this study, the requirement of individual pits needing to be visible was removed, such that other features (i.e. troughs) that had similar physical characteristics to already mapped pit chains, but were missing evidence of individual pits, were later mapped.

To map fractures and faults, the Hillshade tool on `QGIS` was applied to the drone DEM layer and the transparency of the overlaid optical image layer was adjusted to give the image a three-dimensional look. Multiple hillshades were used with the incident angle of illumination changed to better identify fractures and faults oriented at different angles. When mapping, the hillshade that provided the best outline of the feature was used. Vertices were placed along the boundary of each feature from tip to tail to draw out each individual polyline. Similarly to mapping pit craters and pit crater chains, a unique numeric ID was given to each fracture and fault mapped.

S1.2 Geospatial analysis of drone data

The methods for measuring the morphometric properties of each mapped pit crater in this study was also adapted from the methods used by Kling [2020], but with tools in `QGIS` instead of `ArcMap`. To find the area and perimeter length of each pit the 'Add Geometry Attributes' tool was used. Since pit craters are not exactly circular, the length of the major and minor axis was measured using the `'Oriented Minimum Bounding Box'` tool which calculates the smallest rectangle that encompasses each individual pit and returns the dimensions of that

* pritchard@cornell.edu

Editor: E.M. Paguican | Production: G. Seropian

rectangle (all references to pit crater diameter are effectively the length of the major axis). This tool also measures the angle at which that rectangle is oriented with respect to North (0–180 degrees), which is essentially a measurement of the azimuthal orientation of each pit's major axis or diameter. To find the depth of each pit, the `'Zonal Statistics'` tool was used with the pit crater shapefile as the Input Layer and the drone DEM as the Raster Layer to calculate the maximum and minimum elevation of each pit. Pit crater depth was then calculated by finding the difference between the maximum and minimum elevations. Finally, to find the volume, each pit had to be selected individually to clip the drone DEM over the area of the selected pit using the `'Clip Raster by Mask Layer'` tool. Using the `'Raster Surface Volume'` tool, the clipped DEM was then specified as the Input Layer, the Base Level parameter was set to the maximum elevation of the respective pit, and the Method was set to Count Only Below Base Level. The output of this tool was then a maximum estimation of the pit's volume. This series of steps was repeated for each mapped pit, with the results then added to the table of other morphometric measurements in `QGIS`.

Copyright

References

Kling, C. L. (2020). "Pit Craters Throughout the Solar System". PhD thesis. North Carolina State University.

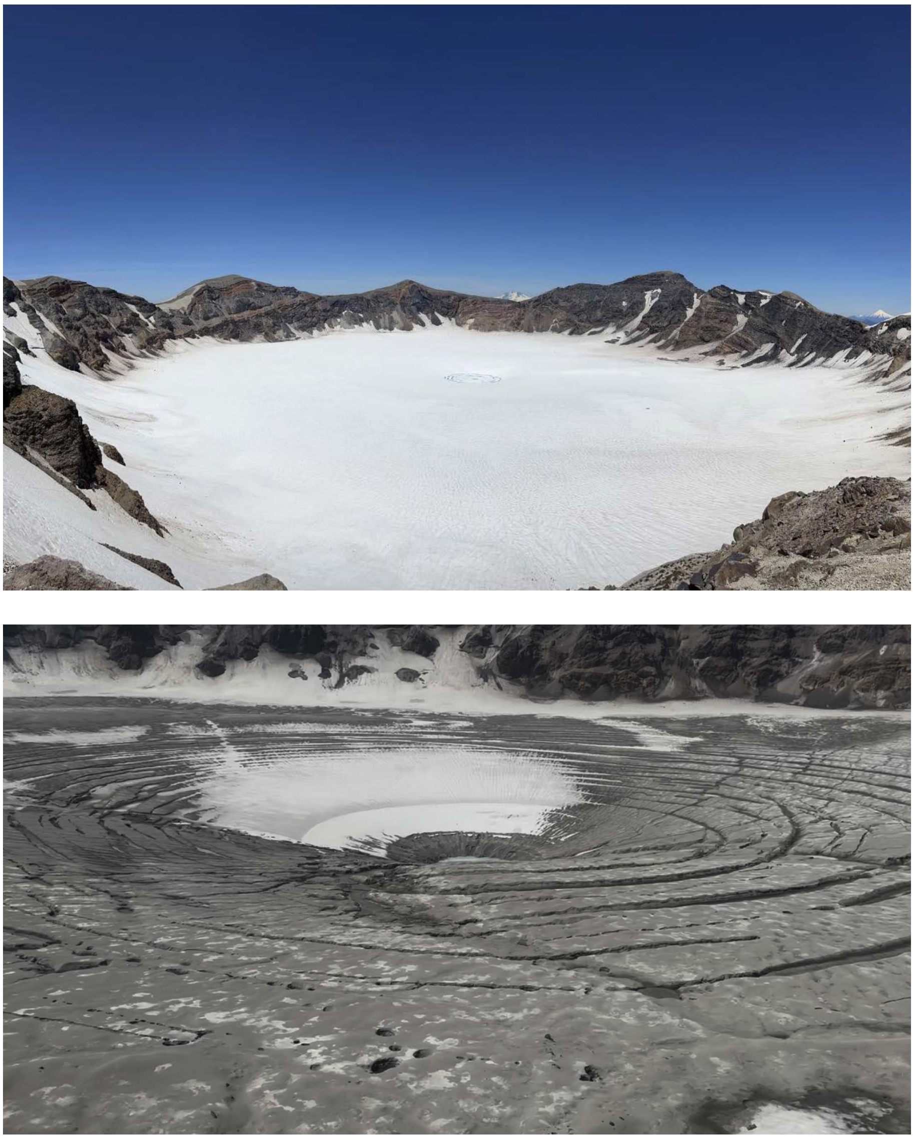

Figure S1: Top: Field photo from January 2025 field season looking into the 2.5 km wide Puyehue summit caldera (courtesy of Matías Calvert Mellado). Note that even though snow covers the entire caldera, the presence of ring fractures still shows up through the snow at the center of the caldera where measured subsidence is the greatest. Bottom: Field photo from January 2026 within the Puyehue summit caldera taken by helicopter looking to the Northeast showing the ring fractures and pit craters more clearly because of the lower snow cover than in 2025.

Table S1: Field measurement of single pit crater diameter on Córdon Caulle laccolith. To assess the accuracy of our measurements of pit crater diameter using the drone data, we took a field-based measurement with a handheld laser rangefinder to measure the length of pit craters encountered in the field. The rangefinder reported distances in units of whole yards (yds) and was not capable of measuring distances less than 15 yds. As a result, the amount of pit craters we were able to measure was significantly limited, which is why only one measurement is reported here. However, the one measurement we did make was in close agreement with our drone based measurement.

ID	Longitude	Latitude	Diameter (m)	Measured length	
				(yds)	(m)
1	-72.1443	-40.5299	20.79	23	21.03

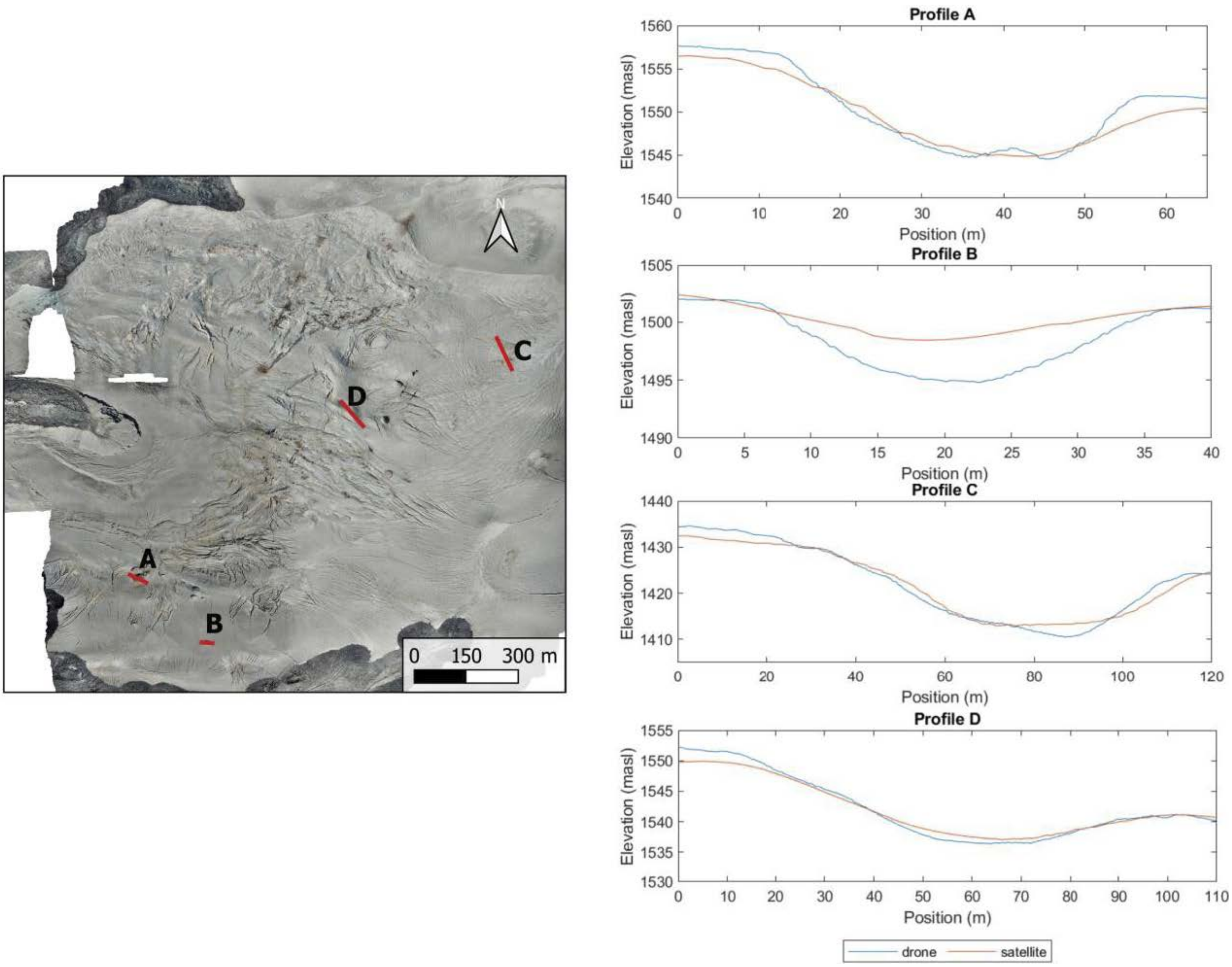

Figure S2: Elevation profiles across four different pit craters on the laccolith using both the drone DEM from March 2022 and the raw 2024 Pléiades satellite DEM (a static offset correction was applied to the satellite DEM to help visualize the comparison). Note elevation profiles A, C, and D yield very similar estimates of pit crater depth and morphology from each DEM. Profile B shows that the agreement between the satellite and drone DEM in not uniform across the laccolith. We found that more significant differences between pit crater depth and morphology estimated from each DEM tended to occur for smaller pit craters. For many of these pits, the Pléiades satellite DEM often showed little to no sign of a depression where a pit crater clearly exists in the optical imagery and in the drone DEM. A possible source of the discrepancy may be due to the difference in spatial resolution of the source optical imagery used to produce each DEM. The very high-resolution drone imagery (4.32 cm/px) may play a role in the ability of the drone DEM to resolve finer scale changes in terrain that does not show up in the satellite DEM.

Table S2: Reported metadata from satellite images used to map pit craters in Figure 6. We include acquisition time in UTC, view angle of sensor in degrees, spatial resolution (mean ground sample distance) in cm, percent of cloud cover in image, and source satellite.

Image date acquisition	Time (UTC)	Mean view angle (°)	Mean GSD (cm)	Cloud coverr (%)	Satellite ID
10-Apr-12	16:08:00	28.3	59.6	0.4	WV02
3-Feb-13	15:46:39	6	47.7	0	WV02
22-Apr-14	15:29:28	22.6	54.5	0.3	WV02
30-Apr-20	18:43:28	27.7	63.2	3.4	WV01

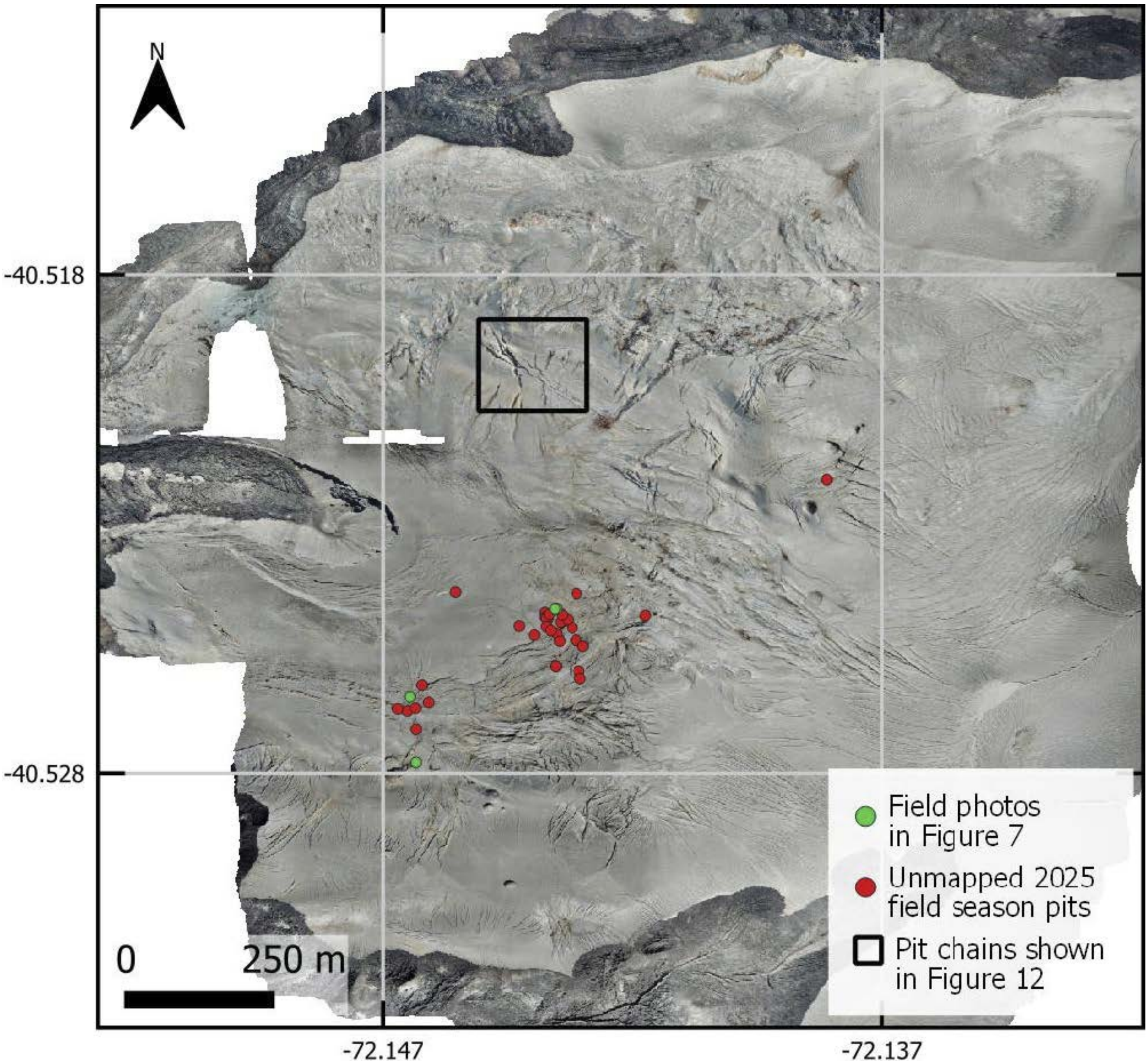

Figure S3: Locations of field photos from Figure 7 in addition to locations of all pits encountered during 2025 field season that were not mapped using 2022 drone image. Black box shows location of pit crater chains in Figure 12.